

# Multireceiver SAS Imagery Based on Monostatic Conversion

Xuebo Zhang , *Member, IEEE*, Haoran Wu , Haixin Sun , *Member, IEEE*, and Wenwei Ying

**Abstract**—To use monostatic based imaging algorithms for multireceiver synthetic aperture sonar, the monostatic conversion is often carried out based on phase centre approximation, which is widely exploited by multireceiver SAS systems. This article presents a novel aspect for dealing with the multireceiver SAS imagery, which still depends on the idea of monostatic conversion. The approach in this article is based on Loffeld's bistatic formula that consists of two important terms, i.e., quasi monostatic and bistatic deformation terms. Our basic idea is to preprocess the bistatic deformation term and then incorporate the quasi monostatic term into an analogous monostatic spectrum. With this new spectrum, traditional imaging algorithms designed for monostatic synthetic aperture sonar can be easily exploited. In this article, we show that Loffeld's bistatic formula can be reduced to the same formula as spectrum based on phase centre approximation when certain conditions are met. Based on our error analysis, the maximum error magnitude of PCA method is about 1 rad, which would noticeably affect the SAS imagery. Fortunately, the error magnitude of presented method can be always kept within  $\pi/4$ . It means that Loffeld's bistatic formula provides a more accurate approximation of the spectrum compared to that based on phase centre approximation. After that, this article develops a new imaging scheme and presents imaging results. Based on quantitative comparisons, the presented method well focuses multireceiver SAS data, and it provides better image compared to phase centre approximation method.

**Index Terms**—Imaging algorithm, Loffeld's bistatic formula, multireceiver, phase error, synthetic aperture sonar.

## I. INTRODUCTION

THE synthetic aperture sonar (SAS) [1]–[5] originates from its counterpart, synthetic aperture radar (SAR) [6]–[10]. Since SAS and SAR works in different environments, the SAS has been developing its own unique style. The multireceiver SAS [1], [2] is mainly developed for mitigating the sampling constraint due to low acoustical propagation velocity. The SAS core task lies in image reconstruction, which typically includes time

and Fourier domain methods. Time domain method [11]–[14] is characterized by the high performance. However, it is computationally inefficient. The efficiency is highly improved using Fourier domain methods [16]–[18], which are further grouped into two classes. For clarity, we suppose that the number of sampling points is  $N_r$  within each emitted pulse. The transmitter emits  $P_{ing}$  pulses, and the receiver array includes  $M$  receivers. Therefore, the total number of sampling points in azimuth is  $N_a = M \cdot P_{ing}$ .

The first type called receiver-by-receiver imagery [1], [2] is to focus a receiver data at a time. Since the multireceiver SAS owns bistatic characteristic, monostatic based algorithms should be extended to focus  $P_{ing} \times N_r$  data. With this method, the multireceiver SAS system is decomposed into  $M$  bistatic SASs. Consequently, the focusing should be repeated  $M$  times. In general, this method would suffer from the disadvantage of maximum latency if parallel algorithms were not used. The other one is to preprocess  $N_a \times N_r$  data, and then apply traditional monostatic SAS imaging algorithms [18]–[22]. Due to this reason, it is called monostatic SAS equivalent method. Before imagery, the preprocessing is required to coerce echo data into monostatic format. Currently, this operation is often conducted via the phase centre approximation (PCA) [18], which is widely used by current multireceiver SAS systems. However, this monostatic conversion would lead to PCA error, which mainly influences the focusing performance at close range [17]. To simplify the signal model, the sonar platform stops when the signal is transmitted and received. After data collection, the sonar moves to next position along the moving direction. We call it the stop-and-hop assumption. However, real sonar moves continuously. That is to say, this assumption would result in stop-and-hop error, which mainly affects the imaging performance at far range [17]. In [22], another imaging method based on modified PCA is presented. The major difference lies in the error term, which is derived by the difference between the two-way range of each receiver and that of reference receiver [23]. In general, the imaging performance is more or less the same with that in [17].

Loffeld's bistatic formula (LBF) [23]–[25] provides a novel aspect for dealing with the spectrum in 2-D frequency domain. Although the method in [24] is based on the assumption that the transmitter and receiver equally contribute to the azimuth modulation, it has good focusing performance for azimuth-invariant configuration. With this method, the spectrum in 2-D frequency domain is expressed as the multiplication of two terms, i.e., quasi monostatic (QM) term and bistatic deformation (BD) term. The

Manuscript received April 11, 2021; revised July 10, 2021 and October 4, 2021; accepted October 15, 2021. Date of publication October 20, 2021; date of current version November 5, 2021. This work was supported in part by National Natural Science Foundation of China under Grant 61971362, in part by the NWN Foundation under Grant 202003101305, and in part by the National Key Laboratory Foundation under Grant 9140C290401150C29132. (*Corresponding author: Xuebo Zhang; Haixin Sun.*)

Xuebo Zhang is with the Northwest Normal University, Lanzhou 730070, China (e-mail: xuebo\_zhang@sina.cn).

Haoran Wu is with the Naval University of Engineering, Wuhan 430030, China (e-mail: wuhaoran\_wh@163.com).

Haixin Sun is with the Xiamen University, Xiamen 361005, China (e-mail: hxsun@xmu.edu.cn).

Wenwei Ying is with the Naval Research Academy, Beijing 102249, China (e-mail: wenwei\_ying@sina.com).

Digital Object Identifier 10.1109/JSTARS.2021.3121405

QM term is similar to monostatic SAS spectrum while the BD term depends on displaced distance between the transmitter and receiver. Therefore, we easily conclude that multireceiver SAS focusing can be converted to monostatic SAS imagery after the compensation of BD term. In this article, we propose an imaging algorithm for the multireceiver SAS system. The presented method still relies on the idea of monostatic conversion. LBF rather than PCA is exploited when the echo data is coerced into monostatic format. We use the range-dependent sub-block post-processing method when it comes to the monostatic conversion. After the compensation of BD term, an analogous monostatic spectrum is obtained. Then, any Fourier based algorithms designed for monostatic SAS can be exploited. This paper mainly focuses on the image reconstruction with range migration algorithm (RMA) [19], [26], [27]. Besides, the comparison between the LBF and PCA, together with phase error analysis in 2-D frequency domain is presented.

Generally speaking, the main contribution of this article lies in four aspects. First, PCA was the only method to conduct monostatic conversion when users wanted to exploit monostatic based imaging algorithms in the past. In this article, we provide a novel method to deal with the monostatic conversion. After this conversion, any Fourier based algorithms designed for monostatic SAS can be directly exploited. Second, since presented method and PCA method are based on the idea of monostatic conversion, there would be internal relationship between both methods. In this article, this relationship is characterized in detail. To some degree, LBF can be reduced to the same formula as spectrum based on PCA method. Third, the phase errors of both methods are analyzed in detail. Based on our analysis, LBF improves spectrum accuracy compared to the PCA method, and it can generate much higher performance of image. Finally, experimental results with better focusing performance validate the high accuracy and effectiveness of presented method.

This article is organized as follows. Section II introduces multireceiver SAS imaging geometry and signal model. Section III presents the LBF, comparison between LBF and PCA, and phase error in 2-D frequency domain. Then, we discuss multireceiver SAS imagery in Section IV. In Section V, simulations and real data are used to validate the presented method. Finally, Section VI concludes this article.

## II. IMAGING GEOMETRY AND SIGNAL MODEL

The multireceiver SAS geometry is shown in Fig. 1(a).  $c$  is the sound speed while  $v$  is the platform velocity. The transducer array has a transmitter and  $M$  receivers aligned in the travelling direction. Each receiver has an integer index  $i \in [1, M]$ . The black rectangle in Fig. 1 denotes the transmitter, and other ones represent the receiver.  $d_i$  is the distance between the  $i$ th receiver and transmitter. Since the SAS system shown in Fig. 1(a) is azimuth invariant, we suppose that an ideal point target is located at coordinates  $(r, 0)$  for clarity.

When the transmitter moves to azimuth position  $v \cdot t$ , the transmitting path  $R_T$  between the transmitter and target is  $R_T(t) = \sqrt{r^2 + (vt)^2}$ , where  $t$  is the slow time. To simplify the geometry modeling, the stop-and-hop assumption is often

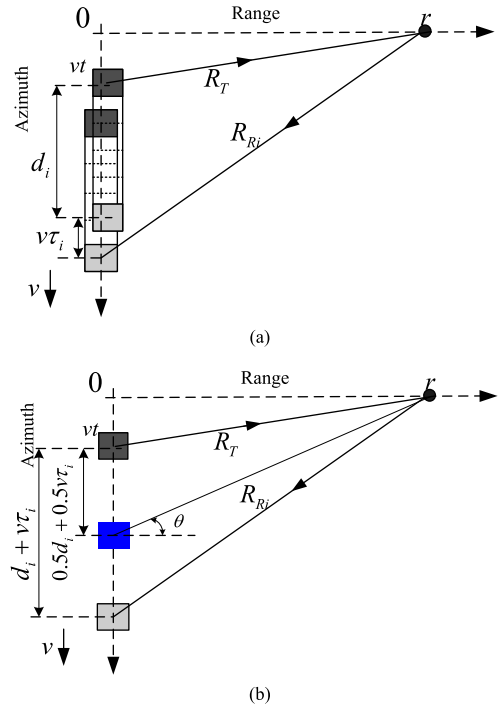


Fig. 1. Imaging geometry of the multireceiver SAS. (a) Imaging geometry. (b) Relationship between transmitter/receiver pair and equivalent transducer.

used. During the data collection, real sonar continuously moves. If we neglect the platform forward distance during the signal propagation time  $\tau_i$  [2], the resultant phase errors degrading SAS imaging performance would become noticeable [28], [29]. Considering the forward distance during the data collection, the receiving path  $R_{Ri}$  between the  $i$ th receiver and target is  $R_{Ri}(t) = \sqrt{r^2 + v^2(t + t_{Ri})^2}$ , where  $t_{Ri} = \tau_i + d_i/v$  represents the azimuth time when the target is seen perpendicularly to the receiver track. The signal propagation time  $\tau_i$  deduced in Appendix A is expressed as

$$\tau_i = \frac{v[(vt-x_0)+d_i]+c\sqrt{(vt-x_0)^2+r^2}}{c^2-v^2} + \frac{\sqrt{\{v[(vt-x_0)+d_i]+c\sqrt{(vt-x_0)^2+r^2}\}^2+(c^2-v^2)[2(vt-x_0)d_i+d_i^2]}}{c^2-v^2} \quad (1)$$

where  $(r, x_0)$  are an arbitrary target coordinates in the imaging area. Here,  $\tau_i$  is approximated by  $\frac{2r}{c \cos \theta}$ . Since this article is also based on the idea of monostatic conversion,  $\theta$  denotes the squint angle between equivalent transducer, and ideal target in Fig. 1(b). In the following part, we would show that LBF is equivalent to PCA. At this point, each bistatic sonar in Fig. 1(a) can be modeled by the transducer located at midpoint between the transmitter and the  $i$ th receiver. That is to say, the bistatic sonar including the black rectangle and gray rectangle in Fig. 1(b) can be approximated by the blue rectangle. From Fig. 1(b),  $\theta$  is calculated by  $\theta = \arctan \frac{vt+0.5d_i+0.5v\tau_i}{r}$ . Inspecting Fig. 1(b), the Doppler frequency introduced by relative moving between equivalent transducer and ideal target is approximately expressed by  $f_t = \frac{2vf_e \sin \theta}{c}$ .

SAS systems often use the wideband signal  $p(\tau)$ . After demodulation, the received signal of the  $i$ th receiver is

$$ss_i(\tau, t) = p\left(\tau - \frac{R_T(t) + R_{Ri}(t)}{c}\right) \omega_a(t) \cdot \exp\left\{-j2\pi f_c \frac{R_T(t) + R_{Ri}(t)}{c}\right\} \quad (2)$$

where  $\tau$  is the fast time in range;  $f_c$  denotes the carrier frequency of transmitted signal;  $\omega_a(\cdot)$  is determined by the transmitter and receiver. Since  $\omega_a(\cdot)$  does not play an important role in our analysis, we suppress this pattern to give more prominence to the phase.

### III. SPECTRUM IN 2-D FREQUENCY DOMAIN

#### A. Spectrum Based on the LBF

Based on Fourier transformation (FT), the method of stationary phase [30] and LBF [24], the spectrum in 2-D frequency domain is given by

$$SS_i(f_\tau, f_t) = P(f_\tau) \exp\{-j\psi(f_\tau, f_t)\} \cdot \exp\left\{-j\frac{\psi_i(f_\tau, f_t)}{2}\right\} \quad (3)$$

with

$$\psi(f_\tau, f_t) = -2\pi f_t \frac{r}{c \cdot \cos\theta} + \frac{4\pi}{c} r \sqrt{(f_c + f_\tau)^2 - f_t^2 \frac{c^2}{4v^2}} \quad (4)$$

$$\psi_i(f_\tau, f_t) = -2\pi f_t \frac{d_i}{v} + \frac{\pi}{c} \frac{(d_i + \frac{2rv}{c \cdot \cos\theta})^2}{(f_c + f_\tau)^2} \cdot \frac{[(f_c + f_\tau)^2 - \frac{f_t^2 c^2}{4v^2}]^{3/2}}{r} \quad (5)$$

In (5), the squint angle  $\theta$  in frequency domain is given by  $\theta = \sin^{-1} \frac{cf_t}{2f_c v}$ .  $f_\tau$  and  $f_t$  are frequency variables corresponding to the fast time  $\tau$  and slow time  $t$ , respectively.  $P(f_\tau)$  is the spectrum of transmitted signal. In Appendix B, we further present the deducing of (3) in detail.

Compared to monostatic SAS, the first term in (4) is a new phase introduced by the stop-and-hop assumption. It would lead to the coordinate deviation in azimuth if this error was not compensated [28]. The second term in (4) is similar to the spectrum of monostatic SAS. Due to this reason, (4) is called the QM term. The term (5) is caused by the spatially displaced elements and stop-and-hop assumption. It describes SAS bistatic feature. At this point, (5) is called the BD term. With the monostatic case, the bistatic feature introduced by the spatial displacement of transmitter/receiver in (5) vanishes. However, there is still bistatic phase caused by the stop-and-hop assumption. It can be neglected when SAS systems are operated with a slow speed or at close range [28].

#### B. Comparison With PCA Method

Here, we show that LBF in Section III-A is an extension of PCA method [17]. Using PCA method [17], the spectrum is

$$SS_i(f_\tau, f_t) = \exp\left\{j2\pi f_t \frac{r}{c} - j4\pi \frac{r}{c} \sqrt{(f_c + f_\tau)^2 - f_t^2 \frac{c^2}{4v^2}}\right\} P(f_\tau) \cdot \exp\left\{j\pi f_t \frac{d_i}{v} - j\pi \frac{(f_c + f_\tau)}{c} \frac{1}{2r} (2\frac{v}{c} r + d_i)^2\right\}. \quad (6)$$

We notice that (6) does not consider the space variance of stop-and-hop error. In general, (6) is similar to (3) except the second exponential term.

The Doppler frequency in azimuth is denoted as  $f_t = \frac{2v(f_c + f_\tau) \sin\theta}{c}$ . Here,  $v \cdot \sin\theta$  is the radial velocity between the sonar and target, and its maximum magnitude is determined by the beam width of transmitter/receiver system. Considering the fact that inequality  $|\sin\theta| \ll 1$  is met, we can obtain  $f_t \ll \frac{2v(f_c + f_\tau)}{c}$  and  $(\frac{cf_t}{2v})^2 \ll (f_c + f_\tau)^2$ . Then, (5) is further reformulated as

$$\begin{aligned} \psi_i(f_\tau, f_t) &= -2\pi f_t \frac{d_i}{v} + \frac{\pi}{c} \frac{(d_i + \frac{2rv}{c \cdot \cos\theta})^2}{(f_c + f_\tau)^2} \frac{[(f_c + f_\tau)^2 - \frac{f_t^2 c^2}{4v^2}]^{3/2}}{r} \\ &\approx -2\pi f_t \frac{d_i}{v} + \frac{\pi}{c} \frac{(d_i + \frac{2rv}{c \cdot \cos\theta})^2}{(f_c + f_\tau)^2} \frac{(f_c + f_\tau)^3}{r} \\ &= -2\pi f_t \frac{d_i}{v} + \pi \frac{(f_c + f_\tau)}{c} \frac{1}{r} \left(2\frac{r}{c \cdot \cos\theta} v + d_i\right)^2. \end{aligned} \quad (7)$$

If we did not consider the space variance of stop-and-hop error in (7), the spectrums shown as (3) and (6) are mostly identical. At this point, we conclude that LBF is just an extension of PCA. The inequality  $f_t \ll \frac{2v(f_c + f_\tau)}{c}$  can be easily satisfied for the SAS system with high frequency. Consequently, this conclusion is just hold for the SAS system with high frequency.

#### C. Phase Error With Short Integration Time

This section discusses the phase error. First of all, the accurate spectrum considered to be the criteria should be calculated. In Appendix B, the expression  $\frac{R_T(t) + R_{Ri}(t)}{c}$  in (32) is replaced by (1). Then, we obtain

$$(f_c + f_\tau) \dot{\tau}_i + f_t = 0 \quad (8)$$

where  $\dot{\tau}_i$  is the first derivative with respect to slow time. Using the bisection method, the numerical root of (8) is obtained, and it is denoted by  $t_{nu\_i}^*$ . The numerical spectrum is

$$\phi_{nu\_i}(f_\tau, t_{nu\_i}^*) = -2\pi (f_c + f_\tau) \cdot \tau_i(t_{nu\_i}^*) - 2\pi f_t \cdot t_{nu\_i}^*. \quad (9)$$

The numerical spectrum accurately considers the influence of stop-and-hop assumption. At this point, (9) is used as the criteria to calculate the phase error. Since the multireceiver SAS configuration is characterized by range variance and azimuth invariance, we fix target azimuth coordinates in the centre of synthetic aperture to discuss the range variance of phase error. The SAS parameters are listed in Table I.

TABLE I  
SAS SYSTEM PARAMETERS

Parameters	Value	Units
centre frequency	150	kHz
bandwidth	20	kHz
platform velocity	3	m/s
receiver length in azimuth	0.04	m
transmitter length in azimuth	0.08	m
pulse repetition interval	0.44	s
number of receivers	66	

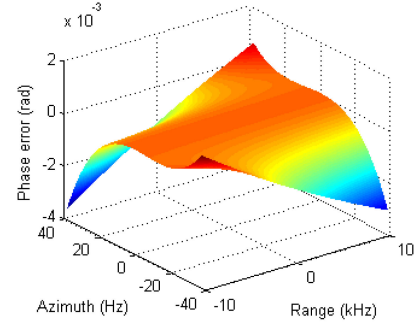
Here, point targets at particular ranges are considered. Target coordinates in range are 50, 135, 220, and 300 m, respectively. Based on (3) and (9), phase errors of the 1st transmitter/receiver pair are shown in Fig. 2.

Inspecting Fig. 2, we draw three conclusions. First, the errors are slight. When  $d_i$  is short, the bistatic SAS is mostly close to monostatic SAS. Consequently, the LBF is close to (9). Second, the error magnitude increases with Doppler frequency away from the Doppler centroid. The transmitter and receiver equally contribute to Doppler when the target is seen perpendicularly to the receiver track. Therefore, the error is nearly zero at this time. Except this time, the error magnitude is increasing due to unequal Doppler contribution of transmitter and receiver. Third, the range variance of error is further discovered based on Fig. 2(a)–(d). The error magnitude is slightly increasing with range. In general, the spectrum shown in (3) suffers from two errors, i.e., LBF error and stop-and-hop error. Here, the LBF error is caused by the approximation including equal Doppler contribution of transmitter/receiver and Taylor expansion, which can be found in the appendix B. When the receiver is close to transmitter, the transmitter/receiver pair can be considered to be a monostatic sonar. Consequently, the LBF error is negligible. At this point, the stop-and-hop error increasing with range is the dominating factor. Therefore, the error increases with range. Generally, the maximal magnitude is just 0.02 rad, which would not noticeably affect the SAS imagery.

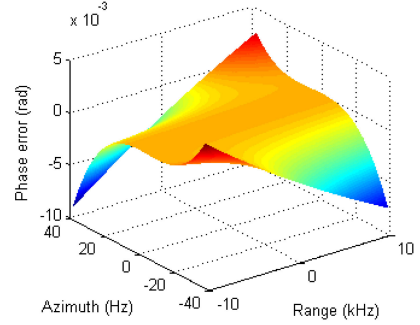
Fig. 3 depicts phase errors for the 66th transmitter/receiver pair under the same condition.

When  $d_i$  is large, we nearly obtain same conclusions described from Fig. 2. However, the error magnitude is decreasing with range by observing Fig. 3(a)–(d). When the receiver is far from transmitter, the equal Doppler contribution of transmitter/receiver and Taylor expansion used in the LBF deducing would lead to noticeable error. That is to say, LBF error is the dominating factor. For targets at far range,  $r$  is much greater than  $d_i$ . At this point, the larger the range  $r$  is, the closer the bistatic SAS is to monostatic one. Comparing Figs. 2 to 3,  $d_i$  has noticeable influence on phase errors. Overall, the maximum magnitude is constrained within  $\pi/4$  [32], which indicates that the LBF can be used for multireceiver SAS imagery.

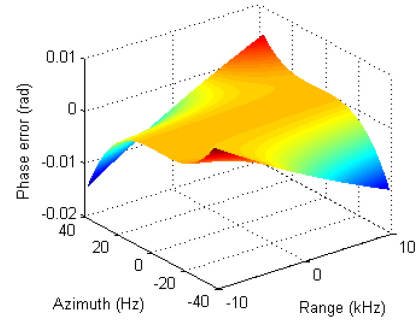
For comparison, Figs. 4 and 5 show phase errors of PCA method for the 1st transmitter/receiver pair and the 66th transmitter/receiver pair, respectively. Based on Fig. 4, the magnitude is still increasing with range  $r$ , as the stop-and-hop error is main factor influencing phase errors. Observing Figs. 2 and 4, the error magnitude of the LBF method is much smaller than that of



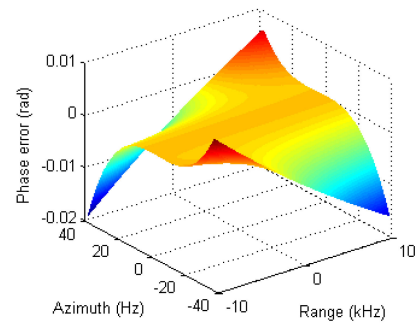
(a)



(b)



(c)

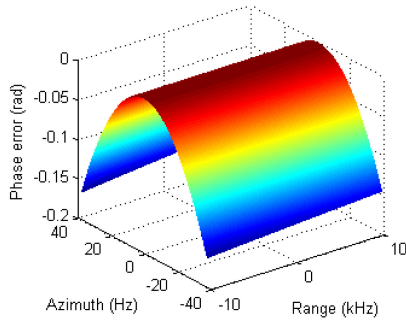


(d)

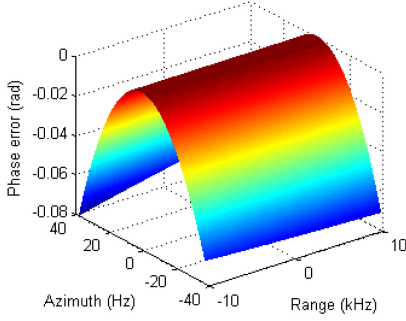
Fig. 2. Phase errors of LBF method for the 1st transmitter/receiver pair. (a)  $r = 50$  m. (b)  $r = 135$  m. (c)  $r = 220$  m. (d)  $r = 300$  m.

PCA method. In general, both methods suffer from negligible error when  $d_i$  is short, and the imaging results would not be noticeably affected.

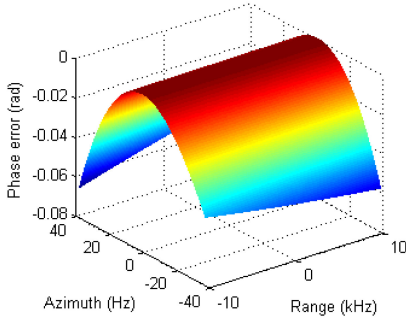
Based on Figs. 3 and 5, the error of PCA method is mostly close to that of presented method when targets are located at close range. Figs. 3(a) and 5(a) further enhances this conclusion.



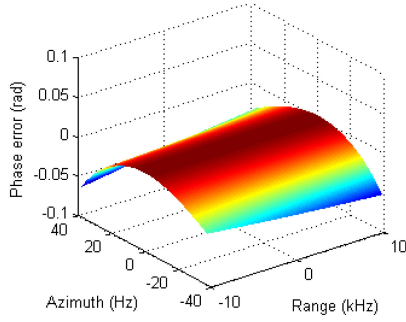
(a)



(b)



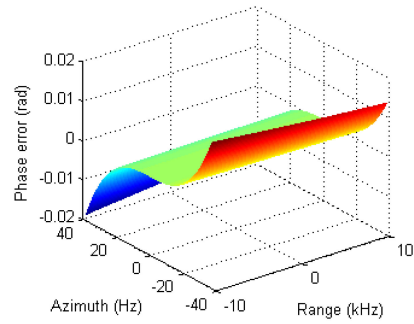
(c)



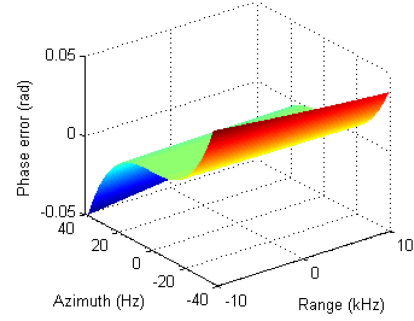
(d)

Fig. 3. Phase errors of LBF method for the 66th transmitter/receiver pair. (a)  $r = 50$  m. (b)  $r = 135$  m. (c)  $r = 220$  m. (d)  $r = 300$  m.

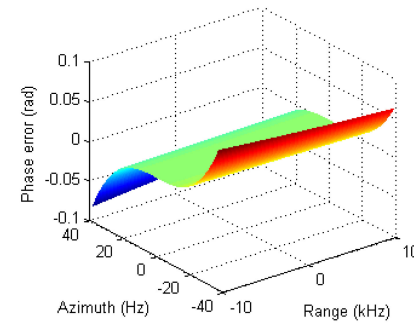
Inspecting Fig. 3(b)–(d), the error of LBF method decreases with range, and the maximum magnitude is about 0.08 rad. However, the error of PCA method slightly increases with range, and the maximum magnitude is 0.15 rad. We consider the azimuth variance of stop-and-hop error in this paper while the PCA method neglects that. Since the stop-and-hop error increases



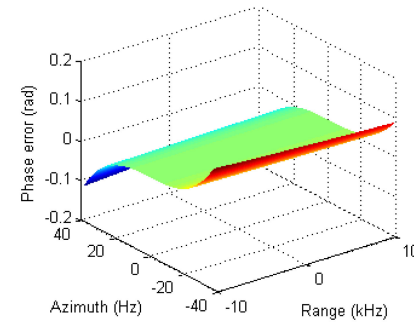
(a)



(b)



(c)



(d)

Fig. 4. Phase error of PCA method for the 1st transmitter/receiver pair. (a)  $r = 50$  m. (b)  $r = 135$  m. (c)  $r = 220$  m. (d)  $r = 300$  m.

with range, the phase error of PCA method shown in Figs. 4 and 5 also increases with range. Therefore, we draw a conclusion that the LBF is slightly superior to PCA method with increasing of range  $r$ . Overall, the comparisons indicate that the LBF in Section III-A slightly improves spectrum accuracy. It means that the LBF would be much closer to numerical one (9).

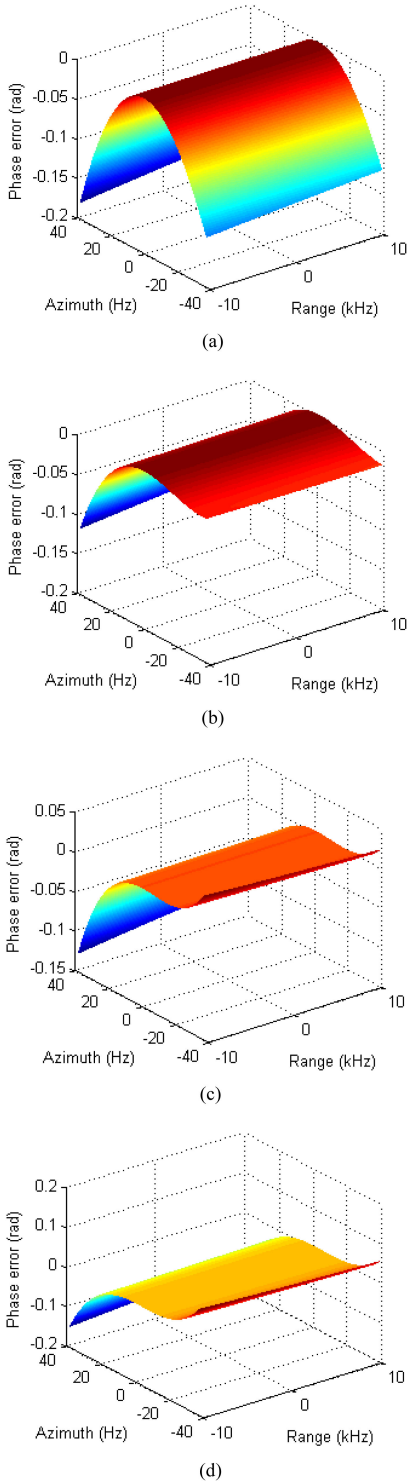


Fig. 5. Phase error of PCA method for the 66th transmitter/receiver pair. (a)  $r = 50$  m. (b)  $r = 135$  m. (c)  $r = 220$  m. (d)  $r = 300$  m.

**D. Phase Error With Long Integration Time**

In this section, we discuss phase errors when the SAS system works with long integration time. The transmitter aperture is 0.04 m in azimuth, and that of receiver is 0.02 m. The receiver array includes 132 receivers. The remaining parameters can be

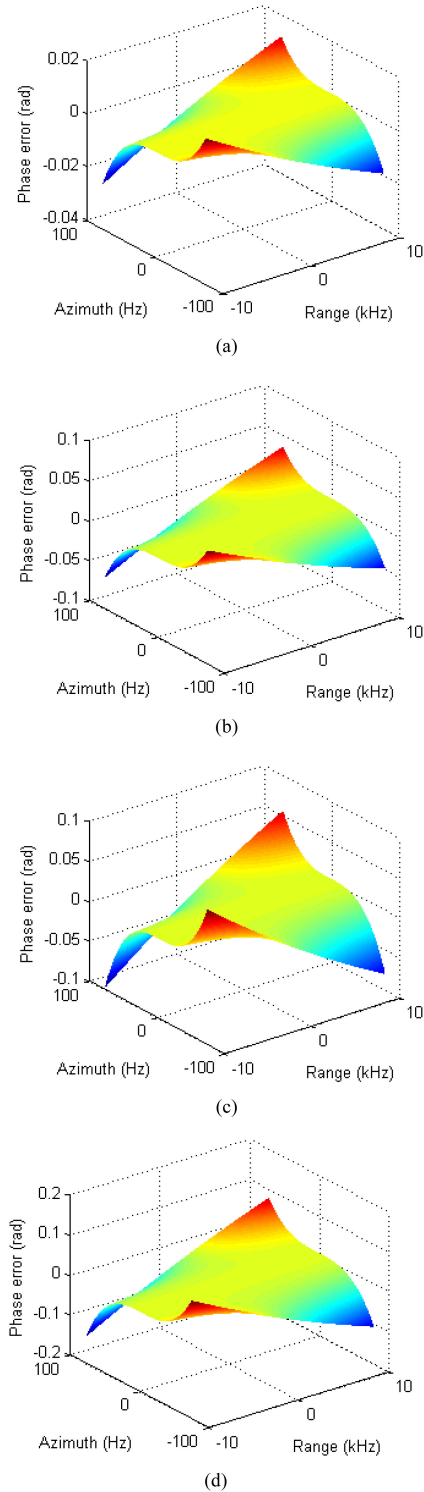


Fig. 6. Phase error of LBF for the 1st transmitter/receiver pair when the system works with long integration time. (a)  $r = 50$  m. (b)  $r = 135$  m. (c)  $r = 220$  m. (d)  $r = 300$  m.

found in Table I. For simplicity, targets used for error simulation in Section III-C are still considered here.

Considering the first receiver/transmitter pair, the phase errors for both methods are depicted in Figs. 6 and 7, respectively. Inspecting Fig. 6(a), the maximum magnitude of presented

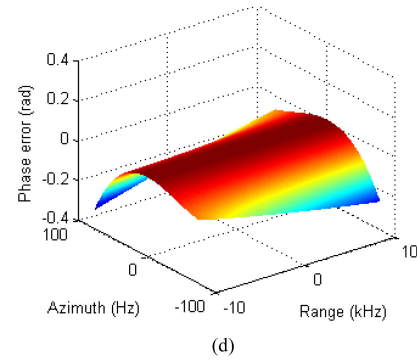
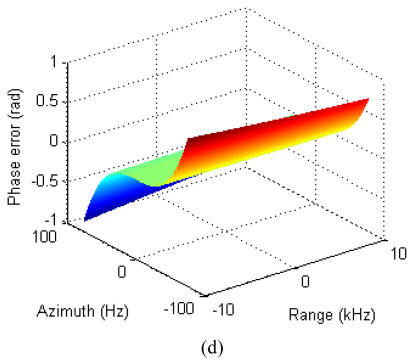
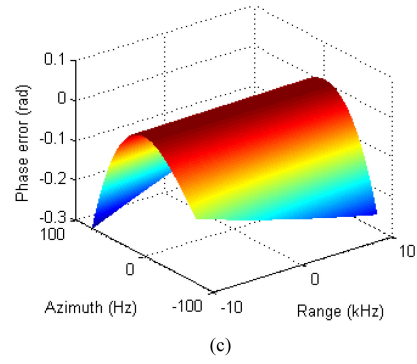
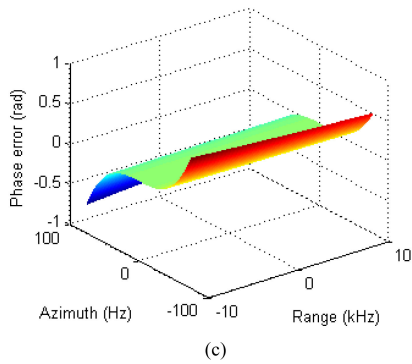
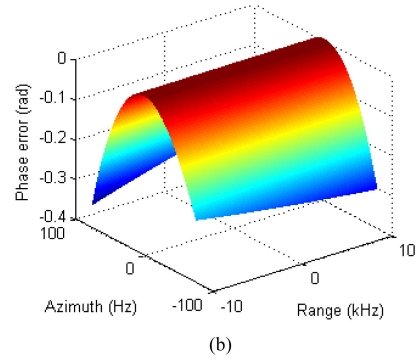
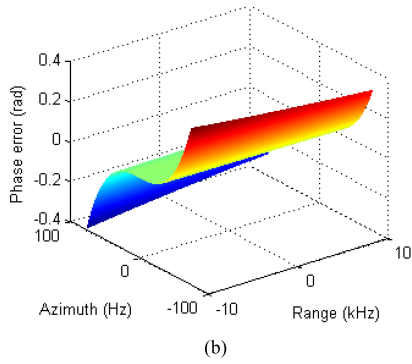
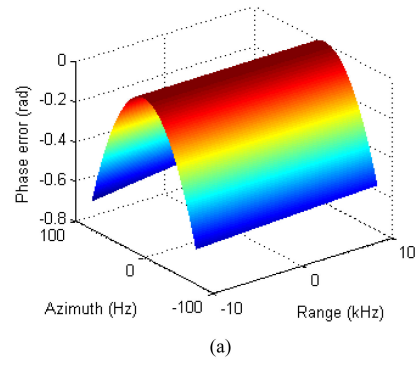
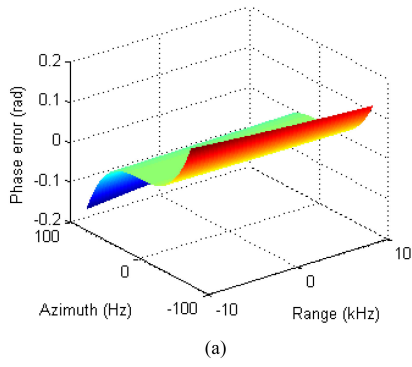


Fig. 7. Phase error of PCA method for the 1st transmitter/receiver pair when the system works with long integration time. (a)  $r = 50$  m. (b)  $r = 135$  m. (c)  $r = 220$  m. (d)  $r = 300$  m.

Fig. 8. Phase error of LBF for the last transmitter/receiver pair when the system works with long integration time. (a)  $r = 50$  m. (b)  $r = 135$  m. (c)  $r = 220$  m. (d)  $r = 300$  m.

method is about 0.02 rad when the targets are at close range. With the increasing of range, the error magnitude increases. In general, there is residual error caused by the stop-and-hop assumption. Fortunately, the maximum magnitude in Fig. 6 is about 0.1 rad, which is less than  $\pi/4$  [31]. From Fig. 7, the

maximum magnitude is about 1 rad, which would noticeably affect the SAS imagery. We can conclude that the spectrum of presented method is superior to that of PCA method.

Considering the last receiver/transmitter pair, we depict the phase errors for both methods in Figs. 8 and 9, respectively.

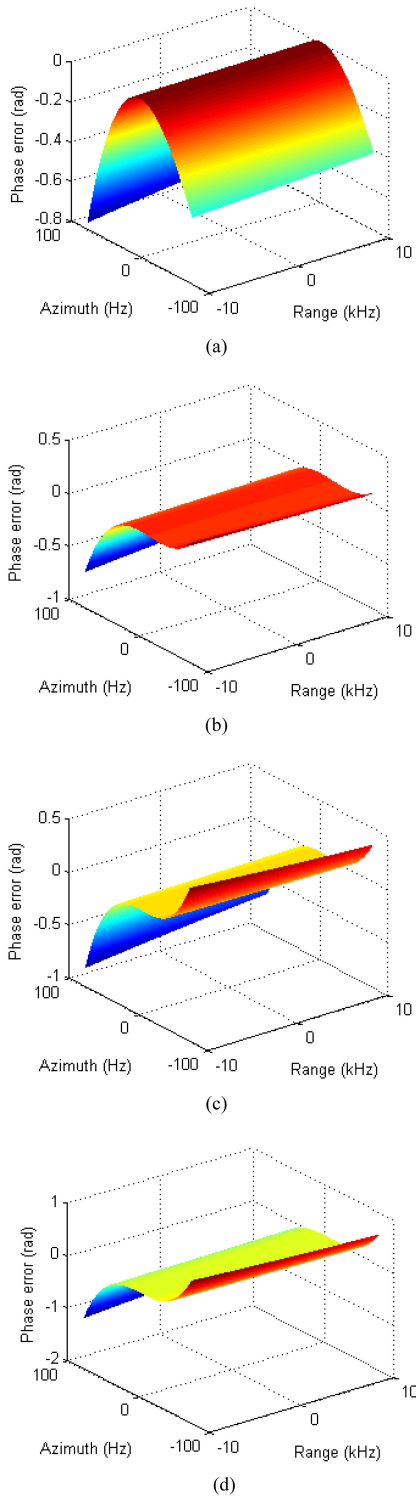


Fig. 9. Phase error of PCA method for the last transmitter/receiver pair when the system works with long integration time. (a)  $r = 50$  m. (b)  $r = 135$  m. (c)  $r = 220$  m. (d)  $r = 300$  m.

Comparing Figs. 8 and 9, the error of presented method slightly decreases with range while that of PCA method increases with range. Generally speaking, our method considers the azimuth variance of stop-and-hop error. However, the PCA method neglects that. Based on Figs. 8 and 9, we find that both

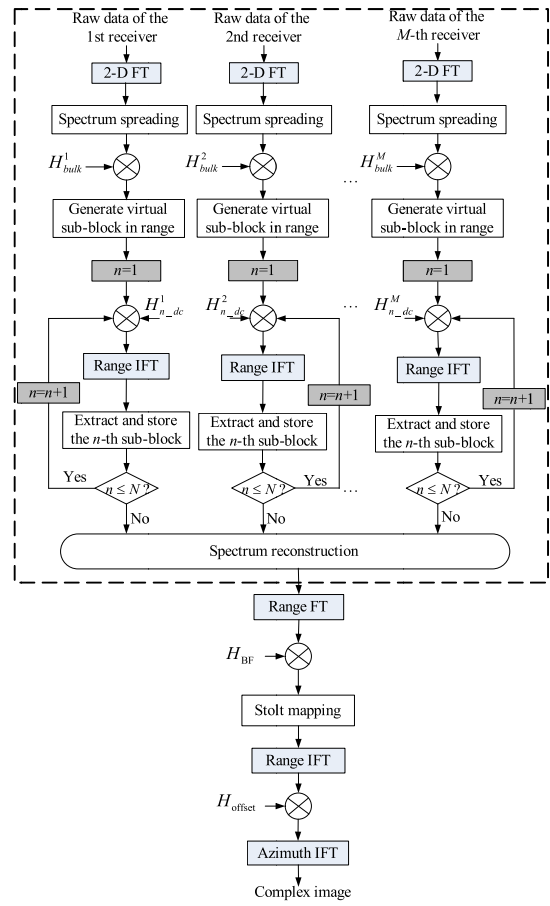


Fig. 10. Block diagram of presented algorithm for multireceiver SAS.

methods nearly obtain the same errors at close range. Figs. 8(a) and 9(a) further enhance this conclusion. Inspecting Figs. 8(d) and 9(d), the error of presented method is smaller than that of PCA method. That is to say, the presented method has the potential to generate higher quality image at far range.

#### IV. IMAGING ALGORITHM FOR MULTIRECEIVER SAS

The preprocessing is often exploited to perform monostatic conversion. Then, the multireceiver SAS data is converted to monostatic equivalent data. Subsequently, any Fourier based imaging algorithms are directly applied without further modifications. This paper takes RMA [19], [26], [27] for example. The block diagram of presented method is shown in Fig. 10.

The dashed area in Fig. 10 denotes preprocessing, which coerces multireceiver SAS data into monostatic format. The preprocessing is presented in Sections IV-A, IV-B, IV-C, and IV-D. The remaining steps describe RMA [19], [26], [27], which is presented in Sections IV-E, IV-F, and IV-G. We first start with preprocessing.

##### A. Spectrum Spreading

Each receiver's data should be transformed into 2-D frequency domain. This spectrum is represented by  $SS_i(f_r, f'_t)$ , where  $f'_t \in [-PRF/2, PRF/2]$  is the Doppler frequency related to



pulse repetition frequency  $PRF$ . The receiver array allows for multiple spatial samples within each pulse [1]. Each receiver is sampled at the  $(1/M)$ th full sampling rate in azimuth. According to the sampling theorem, the spectrum with other frequencies can be obtained by using  $SS_i(f_\tau, f'_t)$  in the fundamental frequency range  $[-PRF/2, PRF/2]$ . This is performed with MATLAB function `repmat()`. The operation is

$$SS_i(f_\tau, f_t) = \text{repmat}(SS_i(f_\tau, f'_t), 1, M). \quad (10)$$

In (10),  $f_t \in [-M \cdot PRF/2, M \cdot PRF/2]$  is the azimuth frequency determined by the full sampling rate  $M \cdot PRF$ .

### B. Bulk Preprocessing

Based on (5), the bulk preprocessing is performed at reference range  $r_{\text{ref}}$ . The filter is given by

$$H_{\text{bulk}}^i(f_\tau, f_t; r_{\text{ref}}) = \text{conj}\{P(f_\tau)\} \exp\left\{j \frac{\psi_i(f_\tau, f_t; r_{\text{ref}})}{2}\right\}. \quad (11)$$

In (11),  $\text{conj}\{\cdot\}$  denotes the conjugated operation. After this step, the signal is compressed in range. Besides, the bistatic feature of echoed signal at reference range is completely cancelled. However, targets not located at reference range suffer from residual errors, which are determined by the phase difference between (5) and (11).

### C. Differential Preprocessing

The range-dependent sub-block postprocessing method is exploited to compensate residual errors. Each receiver's data are virtually divided into several sub-blocks in range. The differential preprocessing function related to each sub-block is

$$H_{n\_dc}^i(f_\tau, f_t; r_{\text{ref}_n}) = \exp\left\{j \frac{\psi_i(f_\tau, f_t; r_{\text{ref}_n})}{2} - j \frac{\psi_i(f_\tau, f_t; r_{\text{ref}})}{2}\right\}. \quad (12)$$

In (12), the block index is represented by the subscript  $n$  ( $1 \leq n \leq N$ ). Here,  $N$  is the total number of blocks in range.  $r_{\text{ref}_n}$  denotes the center range of the  $n$ th sub-block in range. The virtual segmentation is only used for the deduction of differential preprocessing function.

After differential preprocessing for the  $n$ th sub-block, the data are transformed into the range-Doppler domain by range inverse FT (IFT). Then, the  $n$ th sub-block is extracted and stored in order. When the differential preprocessing related to  $N$  sub-blocks is completed, all sub-blocks are coerced into a new signal matrix. It should be noted that our method segments the data after the compensation of phase errors. Therefore, we call it the range-dependent sub-block postprocessing method.

Within each sub-block, the residual phase error after differential preprocessing should be kept within  $\pi/4$  [31]. Under this condition, the imaging performance cannot be affected dramatically. We consider the  $n$ th sub-block in range. The width of the sub-block is  $\Delta r$ . The maximal range and minimal range of the  $n$ th sub-block are  $r_{\text{ref}_n} + 0.5\Delta r$  and  $r_{\text{ref}_n} - 0.5\Delta r$ ,

respectively. Based on (3) and (5), the constraint is

$$\frac{|\psi_i(f_\tau, f_t; r \pm 0.5\Delta r) - \psi_i(f_\tau, f_t; r_{\text{ref}_n})|}{2} < \pi/4. \quad (13)$$

Based on (13), we calculate the total number of sub-blocks in range. Consequently, the width of sub-block can also be obtained.

### D. Spectrum Reconstruction

For each receiver's data, the BD term must be corrected. Then, spectrums of all receiver data are combined to recover monostatic equivalent spectrum. This operation is

$$sS(\tau, f_t) = \sum_{i=1}^M sS_i(\tau, f_t). \quad (14)$$

With this step, the recovered spectrum satisfies the full sampling rate  $M \cdot PRF$ . The recovered data  $sS(\tau, f_t)$  is considered to be the input of monostatic RMA. Next, we concentrate on RMA [19], [26], [27].

### E. Bulk Focusing

When the spectrum reconstruction is performed, the signal is transformed into 2-D frequency domain. The monostatic RMA is applied. Bulk focusing (BF) [19], [26], [27] is first performed to focus targets at reference range  $r_s$ . The filtering function is written as

$$H_{\text{BF}}(f_\tau, f_t; r_s) = \exp\left\{j \frac{4\pi}{c} r_s \sqrt{(f_c + f_\tau)^2 - f_t^2 \frac{c^2}{4v^2}}\right\}. \quad (15)$$

After this step, targets not located at reference range are partially focused due to the mismatch of filtering function.

### F. Stolt Mapping

Residual errors related to targets away from reference range are compensated using Stolt mapping [19], [26], [27], which is

$$f_r = \sqrt{\left(\frac{2\pi f_\tau + 2\pi f_c}{c/2}\right)^2 - \left(\frac{2\pi f_t}{v}\right)^2} - \frac{2\pi f_c}{c/2}. \quad (16)$$

Actually, Stolt mapping is a coordinate transformation, which is a nonlinear mapping of range-frequency variable  $f_\tau$  into a new range-frequency variable  $f_r$ . With this operation, the range-variant range cell migration, range-azimuth coupling, and azimuth modulation are simultaneously compensated.

### G. Azimuth Offset Correction

The first term in (4) is introduced by the stop-and-hop assumption. It would lead to coordinate offset in azimuth if it was not corrected. The data are first transformed into the range-Doppler domain, and the error of stop-and-hop approximation is corrected by

$$H_{\text{offset}}(f_t; r) = \exp\left\{-j2\pi f_t \frac{r}{c \cdot \cos\theta}\right\}. \quad (17)$$

The high-resolution image is obtained by performing an azimuth IFT.

The presented method also needs preprocessing, which is exploited by PCA based method. Due to the range variance of BD term in 2-D frequency domain, the range-dependent sub-block postprocessing rather than interpolation is exploited. The focusing time highly relies on the efficiency of preprocessing, which mainly exploits the FT, IFT, and complex multiplication. For each receiver's data, the compensation of BD term is independently performed. For a particular receiver's data, the differential preprocessing is also independently conducted. Therefore, both operations can be optimized by parallel algorithms like graphics process unit [32] and fastest Fourier transform in the west [33].

## V. DATA PROCESSING RESULTS

This section validates presented method based on simulations and real data. It should be noted that rectangle windows are used in both dimensions with our simulations.

### A. Influence of Sub-Block Width on Imagery

With preprocessing, the presented method compensates the BD term using sub-block processing method. At this point, the sub-block width plays an important role in imaging performance. Based on various sub-block widths, we mainly discuss the imaging performance of presented method. Although time domain back projection (BP) [11]–[14] is characterized by computational load, it provides the high-resolution image. Therefore, the BP based result [13] is used as the criteria to evaluate the performance of presented method. Since the presented method and PCA method [17] belong to the monostatic based method, the comparisons between both methods are mainly conducted.

For clarity, we suppose that a point target is located at coordinates (260 m, 16 m). To simplify simulations, the differential preprocessing functions based on various reference ranges are used to perform differential preprocessing. The difference between the target range and reference range denotes the half width of sub-block. By comparing the imaging performance, the optimal sub-block width is found. Using various sub-block widths, azimuth slices are shown in Fig. 11.

Observing Fig. 11(a), the target suffers from large residual errors when the wide sub-block is used. The result is improved by decreasing the sub-block width. Fig. 11(b), (c), and (f) enhances this conclusion. In Fig. 11(b), the sub-block width  $\Delta r$  is 18 m. The result is clearly improved in comparison with Fig. 11(a). Inspecting Fig. 11(c), (d), and (e), the imaging performance of presented method is mostly close to that of PCA method. Therefore, we conclude that the optimal sub-block width is about 10 m. When a narrower sub-block is used, the result shown in Fig. 11(f) is slightly improved.

We enlarge the area covered by the azimuth resolution, and the results are shown in Fig. 12. Inspecting Fig. 12, we find that the azimuth resolution is not affected by the sub-block width. Based on Figs. 11 and 12, we conclude that the sub-block width does affect the sidelobes of azimuth slice.

To quantify the performance of presented method, the peak sidelobe ratio (PSLR) and integrated sidelobe ratio (ISLR) are used as the quality criteria [19]. PSLR defined by the ratio

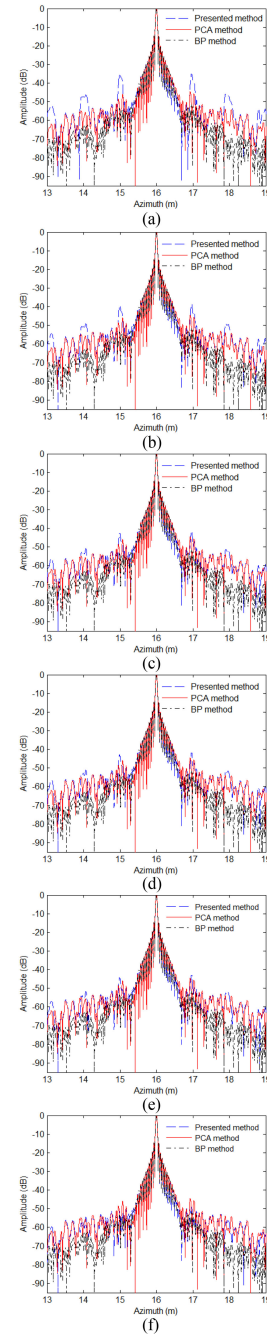


Fig. 11. Azimuth slices of a point target. (a)  $\Delta r = 30.0$  m. (b)  $\Delta r = 18.0$  m. (c)  $\Delta r = 12.0$  m. (d)  $\Delta r = 11.4$  m. (e)  $\Delta r = 9.6$  m. (f)  $\Delta r = 2.7$  m. With the PCA method, the preprocessing is mainly carried out by using complex multiplication and interpolation. Therefore, the approximation error can be well compensated. When it comes to our method, the preprocessing is conducted based on sub-block processing method, which would result in residual phase error for target not at reference range. When the sub-block is large, the performance of presented method is inferior to that of PCA method. That is why we should discuss the optimal sub-block width.

between the largest sidelobe level  $I_{\text{side}}$  and the peak mainlobe level  $I_{\text{main}}$  is given by

$$\text{PSLR} = 10 \log_{10} \frac{I_{\text{side}}}{I_{\text{main}}}. \quad (18)$$

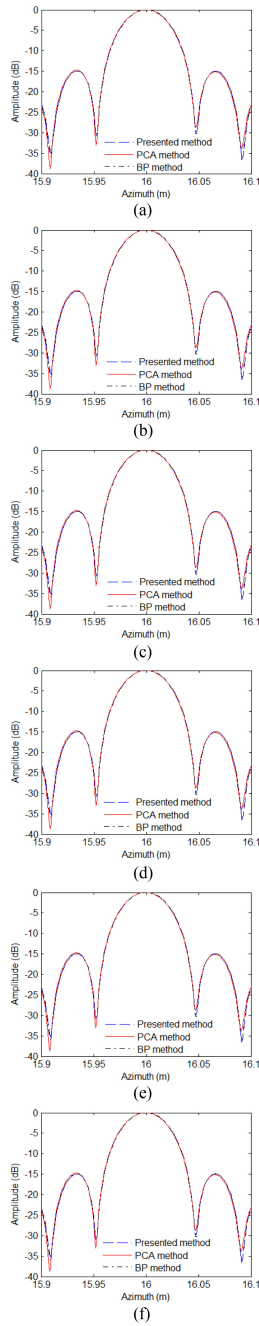


Fig. 12. Azimuth resolution. (a)  $\Delta r = 30.0$  m. (b)  $\Delta r = 18.0$  m. (c)  $\Delta r = 12.0$  m. (d)  $\Delta r = 11.4$  m. (e)  $\Delta r = 9.6$  m. (f)  $\Delta r = 2.7$  m.

Here,  $I$  denotes the intensity of the azimuth slice. PSLR represents the sonar's ability to differentiate a weak target from a nearby strong one.

ISLR defined by the ratio between the total sidelobe power ( $\sum I - \sum_{-3dB} I$ ) and the mainlobe power  $\sum_{-3dB} I$  is expressed as

$$ISLR = 10 \log_{10} \frac{\sum I - \sum_{-3dB} I}{\sum_{-3dB} I}. \quad (19)$$

TABLE II  
QUALITY PARAMETERS WITH THREE IMAGING METHODS

The imaging methods	PSLR/ dB	ISLR/ dB
$\Delta r = 30.0$ m	-14.83	-10.36
$\Delta r = 18.0$ m	-14.85	-10.37
$\Delta r = 12.0$ m	-14.91	-10.40
$\Delta r = 11.4$ m	-14.91	-10.42
$\Delta r = 9.6$ m	-14.93	-10.43
$\Delta r = 2.7$ m	-14.94	-10.44
PCA method	-14.75	-10.42
BP algorithm	-14.94	-10.45

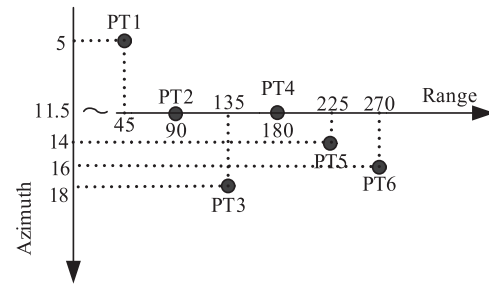


Fig. 13. Simulated scene with six ideal targets.

Here,  $\sum$  denotes the summation operation. ISLR characterizes the ability to detect weak targets in the neighborhood of bright targets.

After computing, PSLR and ISLR are shown in Table II. From Table II, the presented method based on six sub-block widths mostly has the same PSLR and ISLR, as the lower sidelobes slightly affect both quality parameters. Fig. 11 further strengthens this conclusion. If the sub-block was very wide, the PSLR and ISLR would be seriously affected. Generally, we improve the imaging performance by decreasing the sub-block width  $\Delta r$ . Considering sub-block widths with 12.0, 11.4, and 9.6 m, the performance of three cases is mostly identical. That is to say, the optimal sub-block width is about 10 m. If we further decrease the sub-block width, the slight improvement is obtained. The last case related to sub-block width of 2.7 m enhances this conclusion. To balance the performance and efficiency, the optimal sub-block width of 10 m is more preferred when presented method is used.

### B. Imagery With Short Integration Time

We now focus on the imaging performance of presented method across the whole swath. The simulated scene consisting of 6 point targets is shown in Fig. 13. The point targets are marked by PT1, PT2, PT3, PT4, PT5, and PT6 in order.

The data are also focused by the PCA method [17], presented method and BP method [13]. With RMA, the reference range used by the bulk focusing is 40 m. After focusing, the imaging results are shown in Fig. 14.

From Fig. 14(a), the presented method can well reconstruct targets compared to Fig. 14(b) and (c). The azimuth slices depicted in Fig. 15 are depicted to compare the imaging performance. It can be clearly found from Fig. 15 that the curves of presented method agree well with curves of PCA and BP methods. In other words, the conclusion that the presented method can well reconstruct targets is further enhanced.

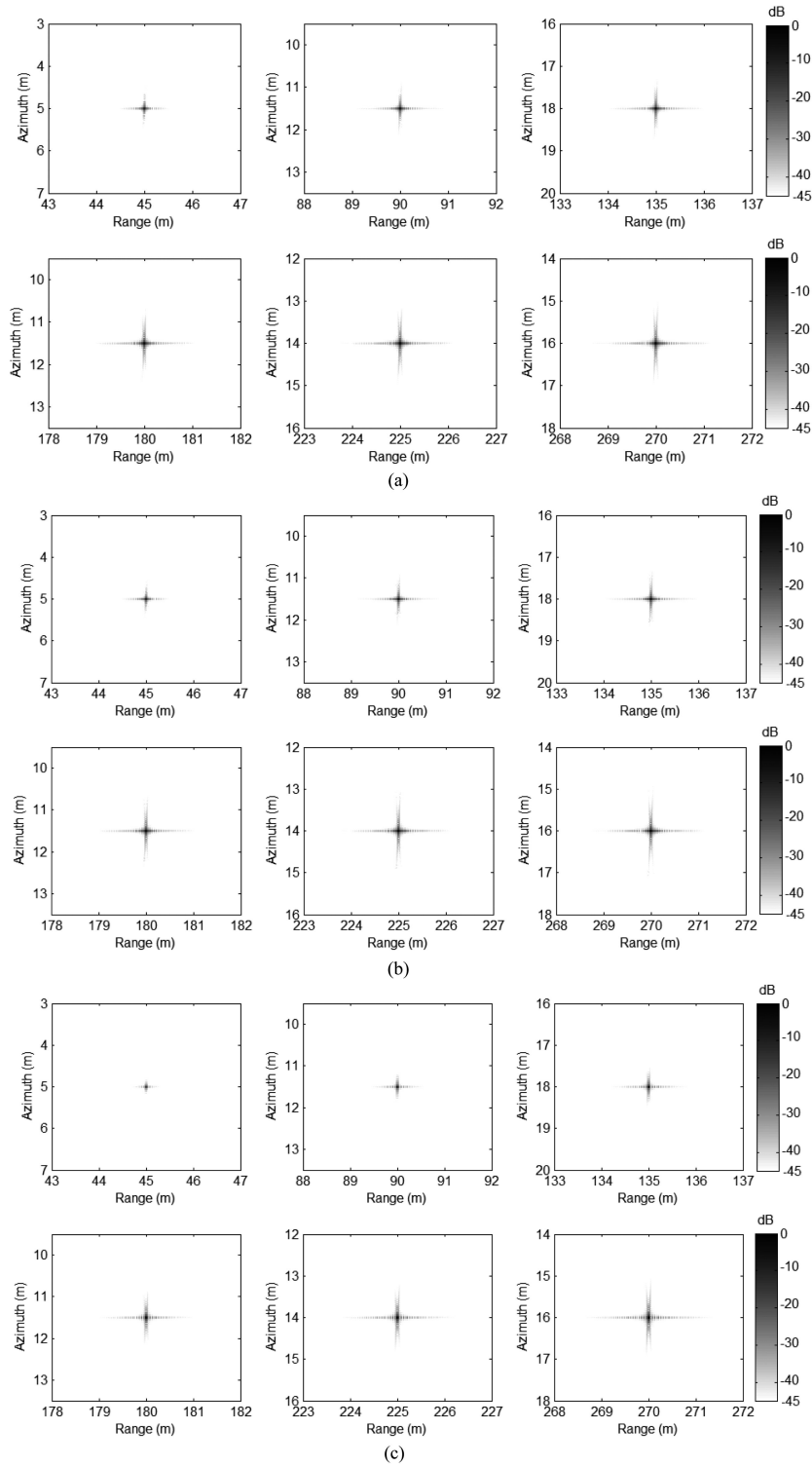


Fig. 14. Imaging results with six ideal targets. (a) Presented method. (b) PCA method. (c) BP algorithm.

To quantitatively evaluate the imaging performance, Table III lists the PSLR and ISLR.

PT1 and PT2 are located at close range. Inspecting PT1 and PT2 in Table III, the PSLR and ISLR with presented method differ from values of BP algorithm by less than 0.29 dB and 0.13 dB, respectively. In general, LBF is suitable for SAS configuration with a low ratio of  $d_i/r$  [34]. Under this case, the bistatic sonar

is much closer to monostatic sonar. Consequently, the approximation error introduced by LBF is slight. The approximation error introduced by LBF would degrade the imaging result, as the ratio  $d_i/r$  is large at close range. For PT1 and PT2, the maximum deviations of PSLR and ISLR between PCA and BP methods are 0.38 dB and 0.17 dB, respectively. Generally, the PCA method suffers from both approximation errors, i.e., PCA error [17] and

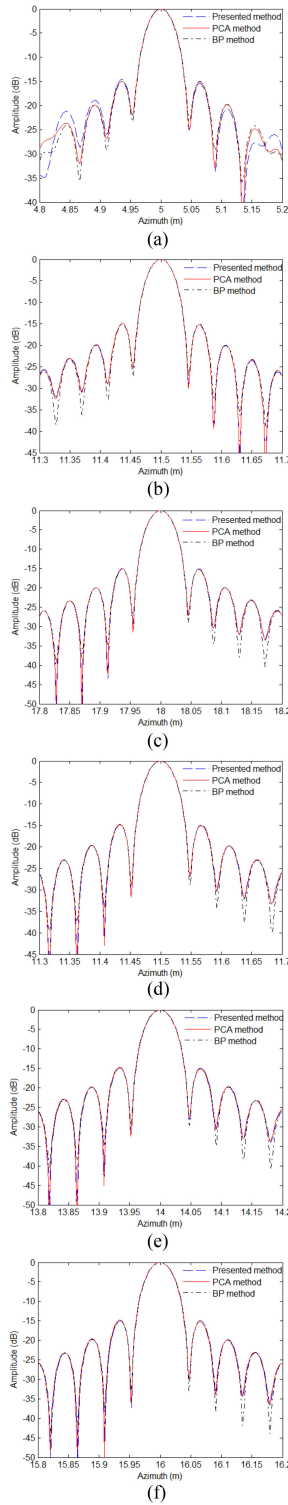


Fig. 15. Azimuth slices. (a) PT1. (b) PT2. (c) PT3. (d) PT4. (e) PT5. (f) PT6.

stop-and-hop error [28]. The PCA error is generated when the transmitter and receiver are replaced by transducer located at the midpoint between the receiver and transmitter. This error mainly affects results at close range. The remaining targets are located at far range. The maximum deviation of PSLR between our method and BP algorithm is 0.04 dB while the maximum deviation

 TABLE III  
 QUALITY PARAMETERS WITH BP, PCA, AND PRESENTED METHODS

	Presented method		PCA method		BP method	
	PSLR / dB	ISLR / dB	PSLR / dB	ISLR / dB	PSLR / dB	ISLR / dB
PT1	-14.72	-10.41	-14.63	-10.37	-15.01	-10.54
PT2	-15.02	-10.94	-14.98	-10.93	-15.11	-11.07
PT3	-15.11	-11.10	-15.03	-11.06	-15.13	-11.20
PT4	-14.90	-10.07	-14.76	-10.05	-14.90	-10.13
PT5	-14.89	-10.32	-14.69	-10.30	-14.93	-10.38
PT6	-14.96	-10.56	-14.75	-10.53	-14.97	-10.61

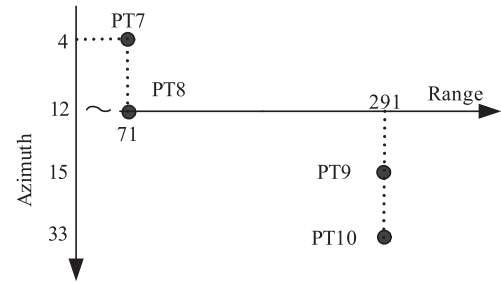


Fig. 16. Target layout for the simulation when the SAS system works with long integration time.

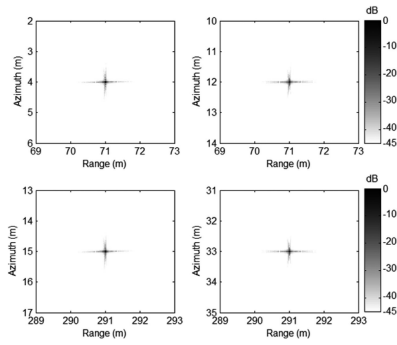
of ISLR is just 0.1 dB. Therefore, we conclude that presented method well focuses targets, as the far range can easily satisfy the demand of low ratio  $d_i/r$ . The maximum deviation of PSLR between PCA and BP algorithms is 0.24 dB while the maximum deviation of ISLR is just 0.14 dB. At far range, the residual stop-and-hop error would degrade imaging results. In general, the presented method slightly outperforms PCA method, and possesses little loss of focusing performance compared to the BP method. This conclusion is consistent with errors shown in Figs. 2–5. Thus, we draw a conclusion that the proposed method obtains high-performance results across the whole swath.

### C. Imagery With Long Integration Time

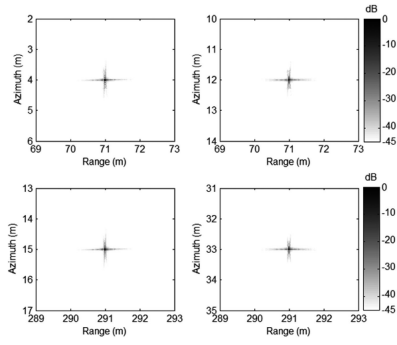
We now focus on the imaging performance when the system works with long integration time. The SAS parameters can be found in Section III-D. We suppose that there four ideal targets, which are shown in Fig. 16.

The presented method, PCA method [17] and BP algorithm [13] are still used to reconstruct the targets. Besides, Wu's method in [23] is further used to process the simulated data. After imagery, the imaging results are shown in Fig. 17. Based on Fig. 17(a), we find that the targets are well recovered by using the presented method compared to results of BP algorithm [13] shown in Fig. 17(d). Inspecting Fig. 17(b) and (c), it seems that PCA method and Wu's method [23] can also reconstruct the targets. In practice, the imaging performance of PCA method [17] and Wu's method [22] are degraded, as the imaging results shown in Fig. 17 cannot visually highlight the slight difference of imaging performance.

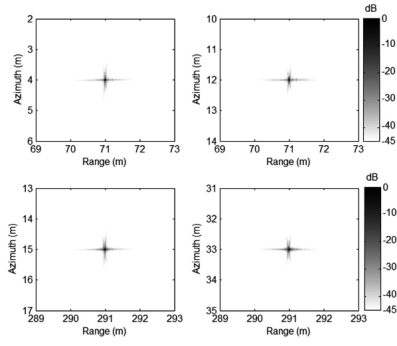
To visually compare the imaging performance, we depict the azimuth slices in Fig. 18. Targets PT7 and PT8 are located



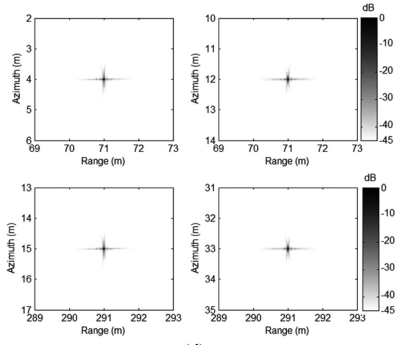
(a)



(b)



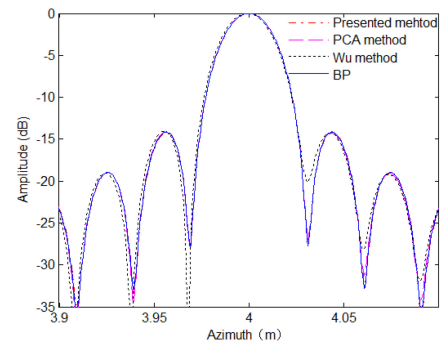
(c)



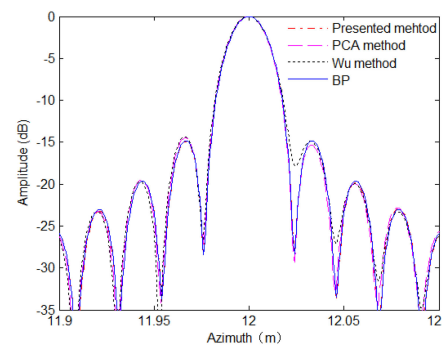
(d)

Fig. 17. Imaging results with four ideal targets. (a) Presented method. (b) PCA method. (c) Wu's method. (d) BP algorithm.

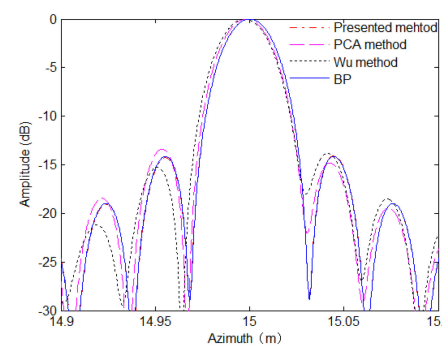
at close range. Therefore, the presented method, PCA method and Wu's method nearly obtain the same focusing performance. Fig. 18(a) and (b) further enhance this conclusion. Targets PT9 and PT10 are at far range. Since presented method provides more accurate spectrum than that of PCA method, the focusing performance of presented method is noticeably superior to that



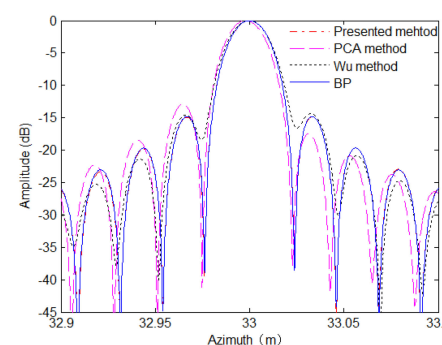
(a)



(b)



(c)



(d)

Fig. 18. Azimuth slices when the SAS system works with long integration time. (a) PT7. (b) PT8. (c) PT9. (d) PT10.

of PCA method at far range. Inspecting Fig. 18(c) and (d), there is the azimuth offset after imagery when PCA method and Wu's method is used. With PCA method and Wu's method, the azimuth offsets for PT9 are about 0.003 m and 0.004 m, respectively. Considering target PT10, the azimuth offsets for

TABLE IV  
QUALITY PARAMETERS WITH FOUR METHODS

	Presented method		PCA method		Wu's method		BP method	
	PSLR/ dB	ISLR/ dB	PSLR/ dB	ISLR/ dB	PSLR/ dB	ISLR/ dB	PSLR/ dB	ISLR/ dB
PT7	-14.13	-6.09	-14.1	-6.07	-14.0	-5.95	-14.18	-6.09
PT8	-14.82	-10.23	-14.47	-10.18	-14.01	-10.14	-14.82	-10.21
PT9	-14.07	-5.83	-13.39	-5.59	-13.81	-5.11	-14.14	-5.83
PT10	-14.83	-10.39	-12.92	-9.74	-14.35	-9.02	-14.84	-10.36

both methods are about 0.002 m. This would lead to distortion for a distributed target. Fortunately, the presented method can successfully solve this problem, and it can provide high-performance image agreeing well with that of BP algorithm. In general, the distortion would occur when PCA method is used for target reconstruction at far range. This conclusion is consistent with that drawn from Figs. 6–9.

PSLR and ISLR shown in Table IV are further exploited to evaluate the focusing performance. Inspecting quality parameters of PT7 and PT8, four methods mostly obtain the same focusing performance. In general, the presented method, PCA method and Wu's method nearly generates the same approximation error when targets are at close range. Inspecting quality parameters of PT9 and PT10, the maximum difference of PSLR and ISLR between presented method and BP algorithm are 0.07 dB and 0.03 dB, respectively. However, the maximum difference of PSLR and ISLR between PCA method and BP algorithm are 1.92 dB and 0.65 dB, respectively. The maximum PSLR with Wu's method differ from that of BP algorithm by 0.81 dB while the maximum ISLR differ from that of BP algorithm by 1.34 dB. Therefore, the presented method is superior to PCA method, and our method can produce high-performance image compared to traditional methods.

#### D. Real Data Processing

In this section, real data are used to validate presented method. The receiver array has 48 receivers evenly spaced over a 1.92 m array. Each receiver has the same along track extent of 0.04 m. The platform is towed at 2.5 m/s. The pulse repetition interval is 0.32 s. The transmitted signal is a chirp, which has a 20 kHz bandwidth at a center frequency of 150 kHz.

The number of sampling points in range is 4096, and that in azimuth is 3200. When real data are divided into 8 sub-blocks in range, the result is shown in Fig. 19(a). Fig. 19(b) is the processing result when there are 16 sub-blocks. Inspecting Fig. 19(a), there are no apparent improvements in Fig. 19(b). It implies that constraints for sub-blocks can be relaxed. In other words, we can use fewer sub-blocks without loss of focusing quality when real data is processed by presented method.

To compare focusing performance, RMA based on PCA method, Wu's method and BP algorithm are still used to process real data. The imaging results are shown in Fig. 20. Inspecting Figs. 19 and 20, we conclude that the presented method can well process the multireceiver SAS data. The experiments also show that our method can obtain high-performance images across the whole swath.

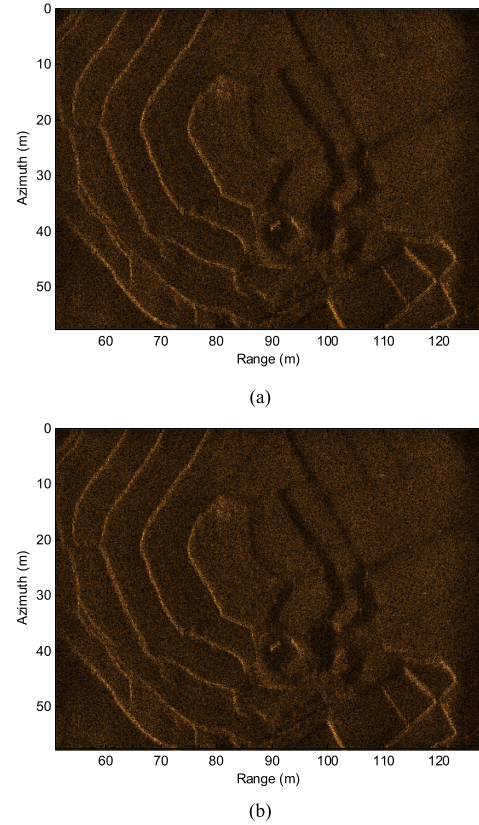


Fig. 19. Imaging results with presented method. (a) 8 sub-blocks. (b) 16 sub-blocks.

We now compare the computational complexity. The number of sampling points in range is denoted by  $N_r$ , while that in azimuth is represented by  $N_a$ . The operations mainly include FT/IFT, complex multiplication, and interpolation. Considering  $N_r$  sampling points, the computation load of FT/IFT is  $1.5N_r \log_2 N_r$ . The SAS data are an  $N_a \times N_r$  matrix. The computation load of FT/IFT in range is  $1.5N_a \cdot N_r \log_2 N_r$  while that in azimuth is  $1.5N_a \cdot N_r \log_2 N_a$ . For phase multiplication, the computation load is  $N_a \cdot N_r$ . Considering the sinc-interpolator with kernel length  $N_{\text{interp}}$ , the computation load is  $(2N_{\text{interp}} - 1)$ . Therefore, the computational loads of these four algorithms are

$$\begin{aligned}
 L_{\text{Proposed}} = & 3(M + 1)N_a \cdot N_r \log_2 N_r + 2(M + 1)N_a \cdot N_r \\
 & + 1.5(M + 1)N_a \cdot N_r \log_2 N_a \\
 & + N_a \cdot N_r (2N_{\text{interp}} - 1)
 \end{aligned} \quad (20)$$

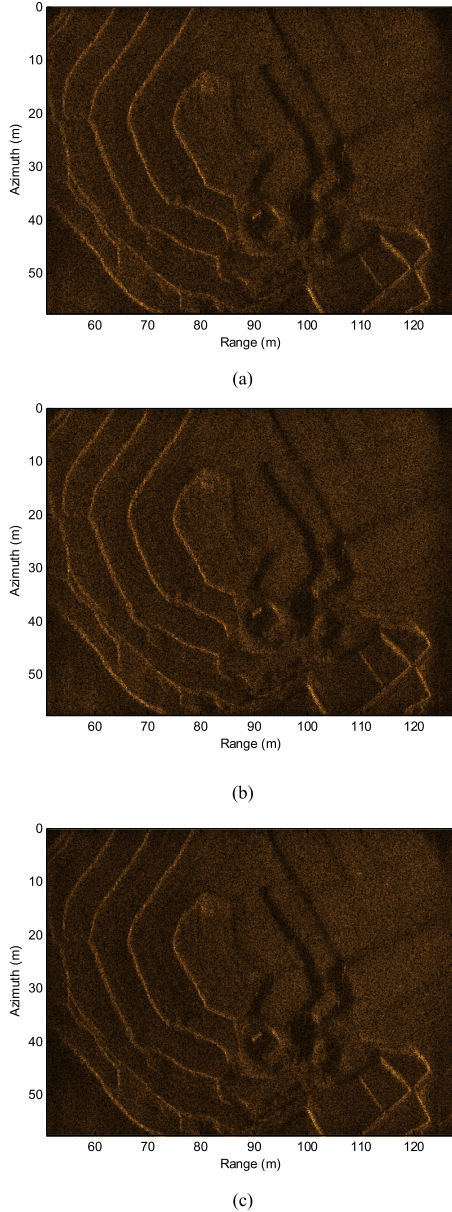


Fig. 20. Processing results of real data. (a) RMA based on PCA method. (b) Wu's method. (c) BP algorithm.

$$\begin{aligned}
 L_{PCA} &= 3(M+1)N_a \cdot N_r \log_2 N_r + (M+2)N_a \cdot N_r \\
 &\quad + 1.5(M+1)N_a \cdot N_r \log_2 N_a \\
 &\quad + 2N_a \cdot N_r (2N_{\text{interp}} - 1) \quad (21)
 \end{aligned}$$

$$\begin{aligned}
 L_{Wu} &= 3(2M+1)N_a \cdot N_r \log_2 N_r + 3N_a \cdot N_r \log_2 N_a \\
 &\quad + 2(M+1)N_a \cdot N_r + N_a \cdot N_r (2N_{\text{interp}} - 1) \quad (22)
 \end{aligned}$$

$$\begin{aligned}
 L_{BP} &= 1.5N_a \cdot N_r \log_2 N_r + N_a \cdot N_r \\
 &\quad + 1.5 \cdot N_a N_{\text{interp}} N_r \log_2 (N_{\text{interp}} N_r). \quad (23)
 \end{aligned}$$

It can be found that BP algorithm is time-consuming. The presented method is much more efficient compared to PCA method, as PCA method needs more operations of interpolation.

TABLE V  
PROCESSING TIME WITH BP, PCA, AND PRESENTED METHODS

	Presented method		PCA method	Wu's method	BP
	8 sub-blocks	16 sub-blocks			
Time/ s	295	547	463	436	5168

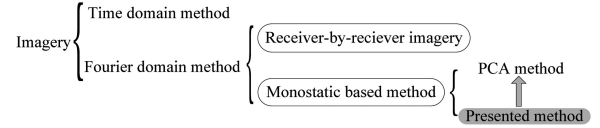


Fig. 21. Categories of multireceiver SAS imaging algorithms.

Both PCA method and Wu's method nearly possesses the same computation load.

The processing time of three methods is further tested. The laptop is installed with Windows 10, 64-bit operating system, 2.6-GHz CPU, 8-GB memory and MATLAB R2012a. The processing time is listed in Table V. It should be noted that our method and PCA method includes monostatic conversion and image focusing. For both methods, the major difference of processing time is caused by the monostatic conversion.

Inspecting Table V, the processing time of PCA method is mostly close to that of Wu's method, as Wu's method is also based on the idea of PCA. After optimization of BP algorithm, many steps can be performed with matrix operation. Thus, the imaging efficiency is dramatically improved, and the processing time is 5168 s. When the data are divided into 8 sub-blocks in range, the processing time with presented method is 295 s. The processing time based on 16 sub-blocks is 547 s. Clearly, it is more time-consuming when the data are divided into much more sub-blocks in range, because more time is needed to perform differential preprocessing. Overall, the efficiency of our method is at least improved 9.45 times in comparison with BP algorithm. The processing efficiency of our method is expected to be further improved by using parallel algorithms.

## VI. CONCLUSION

In general, multireceiver SAS imaging algorithms are summarized in Fig. 21.

Time domain method characterized by computationally inefficiency is viewed as precise method. Its results are usually used as the criteria to evaluate the performance of other methods. Monostatic based method belongs to Fourier domain method. After converting multireceiver SAS data to monostatic equivalent data, this method directly uses monostatic imaging algorithms without further modifications. Thus, the monostatic conversion is an important step. To use monostatic based method, the monostatic SAS spectrum must be decomposed into two parts independently. Summarily, the spectrum in 2-D frequency domain is expressed as

$$\begin{aligned}
 SS_i(f_\tau, f_t) \\
 = P(f_\tau) \exp \{-j\Theta(f_\tau, f_t; r) - j\Theta_i(f_\tau, f_t; r, d_i)\}. \quad (24)
 \end{aligned}$$



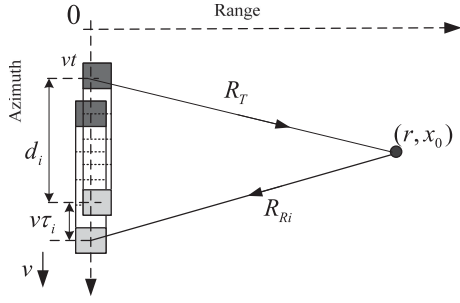


Fig. 22. Imaging geometry between SAS system and an arbitrary target.

In (24),  $\Theta(f_\tau, f_t; r)$  closing to monostatic SAS spectrum is independent of  $d_i$ .  $\Theta_i(f_\tau, f_t; r, d_i)$  highly depends on  $d_i$ . After compensating  $\Theta_i$ , multireceiver SAS data are forced into monostatic equivalent data. In other words, the monostatic conversion based method cannot be applied if multireceiver SAS spectrum was not able to be independently decomposed into  $d_i$  dependent part and  $d_i$  independent part.

Currently, the PCA method is widely used. In this article, we provide a novel aspect for dealing with monostatic conversion. In Fig. 21, the gray part summarizes the main contribution of this article. Based on LBF, the spectrum can be decomposed into the QM term and BD term depending on  $d_i$ . Therefore, the monostatic conversion can be performed by compensating the BD term. The subsequent processing can be simply performed by using monostatic imaging algorithms without further modifications. Furthermore, we construct the relationship between presented and PCA methods. When some certain conditions are met, LBF is approximately equal to PCA method. That is to say, LBF is simplified to PCA based spectrum.

#### APPENDIX A

In this appendix, the derivation for (1) is presented in detail. The imaging geometry is shown in Fig. 22. For clarity, an arbitrary target is supposed to be located at coordinates  $(r, x_0)$  in the imaging area. When the transmitter is located at coordinates  $(0, v \cdot t)$ , the signal is transmitted. At this time, the  $i$ th receiver is just located at coordinates  $(0, v \cdot t + d_i)$ .

When the echo signal received by the  $i$ th receiver, the time delay is supposed to be  $\tau_i$ . During the signal propagation, real sonar continuously moves, and the moving distance of the  $i$ th receiver along the azimuth dimension is  $v \cdot \tau_i$ . That is to say, the  $i$ th receiver is located at coordinates  $(0, v \cdot t + d_i + v \cdot \tau_i)$  when it receives echo signal. The actual path length from transmitter to target and then back to the  $i$ th receiver is given by

$$R_i(\tau, t) = \sqrt{r^2 + (vt - x_0)^2} + \sqrt{r^2 + (vt + d_i + v\tau_i - x_0)^2}. \quad (25)$$

With the time delay  $\tau_i$ , the slant range can be expressed as

$$R_i(\tau, t) = c \cdot \tau_i. \quad (26)$$

Based on (25) and (26), we obtain a formula expressed as a quadratic in terms of  $\tau_i$

$$c \cdot \tau_i = \sqrt{r^2 + (vt - x_0)^2} + \sqrt{r^2 + (vt + d_i + v\tau_i - x_0)^2}. \quad (27)$$

Equation (27) can be further reformulated as

$$(c^2 - v^2) \tau_i^2 - 2\tau_i \left[ c\sqrt{r^2 + (vt - x_0)^2} + v(vt + d_i - x_0) \right] - [2d_i(vt - x_0) + d_i^2] = 0. \quad (28)$$

Since the time delay  $\tau_i$  is the only unknown parameter in (28), we can solve for this using the quadratic formula. The solution to (28) is given by

$$\tau_i = \frac{v[(vt-x_0)+d_i]+c\sqrt{(vt-x_0)^2+r^2}}{c^2-v^2} + \frac{\sqrt{\left\{v[(vt-x_0)+d_i]+c\sqrt{(vt-x_0)^2+r^2}\right\}^2+(c^2-v^2)[2(vt-x_0)d_i+d_i^2]}}{c^2-v^2}. \quad (29)$$

#### APPENDIX B

The signal expressed as (2) is first transformed into range frequency domain, and it is given by

$$Ss_i(f_\tau, t) = P(f_\tau) \exp \left\{ -j2\pi (f_c + f_\tau) \frac{R_T(t) + R_{Ri}(t)}{c} \right\}. \quad (30)$$

FT is then applied to (30), we obtain the 2-D spectrum, which is expressed as

$$SS_i(f_\tau, f_t) = \int_{-0.5T_s}^{0.5T_s} \exp \left\{ -j2\pi (f_c + f_\tau) \frac{R_T(t) + R_{Ri}(t)}{c} \right\} \exp \{-j2\pi f_t t\} dt \times P(f_\tau). \quad (31)$$

Here,  $P(f_\tau)$  is the spectrum of transmitted signal.  $T_s$  is the synthetic aperture time.

Since the term  $[R_T(t) + R_{Ri}(t)]$  in (31) is characterized by double square roots, (31) cannot be analytically integrated. To simplify deducing, we define a new phase term

$$\phi_i = -2\pi (f_c + f_\tau) \frac{R_T(t) + R_{Ri}(t)}{c} - 2\pi f_t t. \quad (32)$$

LBF supposes that the transmitter and receiver contribute equally to the Doppler phase. Equation (32) is further decomposed into two terms expressed as

$$\begin{aligned} \phi_T(f_\tau, t) &= 2\pi \frac{f_c + f_\tau}{c} R_T(t) + \pi f_t t \\ \phi_{Ri}(f_\tau, t) &= 2\pi \frac{f_c + f_\tau}{c} R_{Ri}(t) + \pi f_t t. \end{aligned} \quad (33)$$

Based on the method of stationary phase [31], the points of stationary phase corresponding to (33) is

$$t_T^* = -\frac{crf_t}{2v(f_c + f_\tau)} \cdot \frac{1}{\sqrt{v^2 - \left(\frac{cf_t}{2(f_c + f_\tau)}\right)^2}}$$

$$t_{Ri}^* = -\frac{crf_t}{2v(f_c + f_\tau)} \cdot \frac{1}{\sqrt{v^2 - \left(\frac{cf_t}{2(f_c + f_\tau)}\right)^2}} - \frac{d_i}{v} - \frac{2r}{c \cdot \cos \theta}. \quad (34)$$

Here,  $t_T^*$  and  $t_{Ri}^*$  are the points of stationary phase corresponding to transmitter phase and receiver phase, respectively.

Equation (33) is further expanded up to the second order term around their points of stationary phase. Then, we obtain

$$\begin{aligned} \phi_T(f_\tau, t) &\approx \phi_T(f_\tau, t_T^*) + \phi_T'(f_\tau, t_T^*)(t - t_T^*) \\ &\quad + \frac{1}{2}\phi_T''(f_\tau, t_T^*)(t - t_T^*)^2 \\ \phi_{Ri}(f_\tau, t) &\approx \phi_{Ri}(f_\tau, t_{Ri}^*) + \phi_{Ri}'(f_\tau, t_{Ri}^*)(t - t_{Ri}^*) \\ &\quad + \frac{1}{2}\phi_{Ri}''(f_\tau, t_{Ri}^*)(t - t_{Ri}^*)^2. \end{aligned} \quad (35)$$

Considering the method of stationary phase [31],  $\phi_T'(f_\tau, t_T^*) = 0$  and  $\phi_{Ri}'(f_\tau, t_{Ri}^*) = 0$  are always hold. Based on (35), (32) is reformulated as

$$\begin{aligned} \widehat{\phi}_i &= -\phi_T(f_\tau, t) - \phi_{Ri}(f_\tau, t) \\ &\approx -\phi_T(f_\tau, t_T^*) - \phi_{Ri}(f_\tau, t_{Ri}^*) \\ &\quad - \frac{1}{2}\phi_T''(f_\tau, t_T^*)(t - t_T^*)^2 - \frac{1}{2}\phi_{Ri}''(f_\tau, t_{Ri}^*)(t - t_{Ri}^*)^2 \\ &= \phi_T(f_\tau, t_T^*) - \phi_{Ri}(f_\tau, t_{Ri}^*) \\ &\quad - \frac{\phi_T''(f_\tau, t_T^*) \cdot \phi_{Ri}''(f_\tau, t_{Ri}^*)}{\phi_T''(f_\tau, t_T^*) + \phi_{Ri}''(f_\tau, t_{Ri}^*)} (t_T^* - t_{Ri}^*)^2 \\ &\quad - \left[ \phi_T''(f_\tau, t_T^*) + \phi_{Ri}''(f_\tau, t_{Ri}^*) \right] (t - t_i^*)^2 \end{aligned} \quad (36)$$

with

$$t_i^* = \frac{\phi_T''(f_\tau, t_T^*)t_T^* + \phi_{Ri}''(f_\tau, t_{Ri}^*)t_{Ri}^*}{\phi_T''(f_\tau, t_T^*) + \phi_{Ri}''(f_\tau, t_{Ri}^*)}. \quad (37)$$

Based on (36), (37) and method of stationary phase [31], the point of stationary phase corresponding to  $\widehat{\phi}_i$  is  $t_i^*$ . Substituting  $t_i^*$  into (36) yields

$$\begin{aligned} \widehat{\phi}_i &= -\phi_T(f_\tau, t_T^*) - \phi_{Ri}(f_\tau, t_{Ri}^*) \\ &\quad - \frac{\phi_T''(f_\tau, t_T^*) \cdot \phi_{Ri}''(f_\tau, t_{Ri}^*)}{\phi_T''(f_\tau, t_T^*) + \phi_{Ri}''(f_\tau, t_{Ri}^*)} (t_T^* - t_{Ri}^*)^2. \end{aligned} \quad (38)$$

Substituting (34) into (38) yields

$$\widehat{\phi}_i = -\psi(f_\tau, f_t) - \frac{\psi_i(f_\tau, f_t)}{2} \quad (39)$$

with

$$\begin{aligned} \psi(f_\tau, f_t) &= -2\pi f_t \frac{r}{c \cdot \cos \theta} + \frac{4\pi}{c} r \sqrt{(f_c + f_\tau)^2 - f_t^2 \frac{c^2}{4v^2}} \\ \psi_i(f_\tau, f_t) &= -2\pi f_t \frac{d_i}{v} + \frac{\pi}{c} \cdot \frac{(d_i + \frac{2rv}{c \cdot \cos \theta})^2}{(f_c + f_\tau)^2} \cdot \frac{[(f_c + f_\tau)^2 - f_t^2 \frac{c^2}{4v^2}]^{3/2}}{r}. \end{aligned} \quad (40)$$

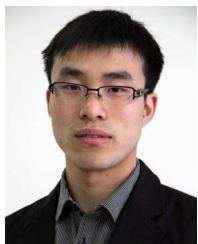
## ACKNOWLEDGMENT

The authors would like to thank the editors and anonymous reviewers for their valuable comments and suggestions that helped improve this paper.

## REFERENCES

- [1] M. Ma, J. Tang, and H. Zhong, "CZT algorithm for multiple-receiver synthetic aperture sonar," *IEEE Access*, vol. 8, pp. 1902–1909, Mar. 2020.
- [2] X. Zhang, C. Tan, and W. Ying, "An imaging algorithm for multireceiver synthetic aperture sonar," *Remote Sens.*, vol. 11, no. 6, Mar. 2019, Art. no. 672.
- [3] C. Cuenca-Garcia *et al.*, "Sensing archaeology in the north: The use of non-destructive geophysical and remote sensing methods in archaeology in Scandinavian and North Atlantic territories," *Remote Sens.*, vol. 12, no. 18, Sep. 2020, Art. no. 3102.
- [4] X. Zhang and P. Yang, "Imaging algorithm for multireceiver synthetic aperture sonar," *J. Electr. Eng. Technol.*, vol. 14, no. 1, pp. 471–478, Jan. 2019.
- [5] C. Cuenca-Garcia *et al.*, "Sensing archaeology in the north: The use of non-destructive geophysical and remote sensing methods in archaeology in Scandinavian and North Atlantic territories," *Remote Sens.*, vol. 12, no. 18, Sep. 2020, Art. no. 3102.
- [6] M. Shang *et al.*, "The space-time variation of phase imbalance for GF-3 azimuth multichannel mode," *IEEE J. Sel. Topics Appl. Earth Observ. Remote Sens.*, vol. 13, pp. 4774–4788, Aug. 2020.
- [7] C. Liu and W. Zhu, "Review of target detection in SAR image based on CNN," *J. Ordnance Equip. Eng.*, vol. 42, no. 3, pp. 15–21, Mar. 2021.
- [8] N. Adam, "Methodology of a troposphere effect mitigation processor for SAR interferometry," *IEEE J. Sel. Topics Appl. Earth Observ. Remote Sens.*, vol. 12, no. 12, pp. 5334–5344, Dec. 2019.
- [9] S. Chauhan, H. S. Srivastava, and P. Patel, "Crop height estimation using RISAT-1 hybrid-polarized synthetic aperture radar data," *IEEE J. Sel. Topics Appl. Earth Observ. Remote Sens.*, vol. 12, no. 8, pp. 2928–2933, Aug. 2019.
- [10] J. Amao-Oliva, D. Torres-Roman, I. Yanez-Vargas, A. Reigber, and M. Jager, "The Beltrami SAR framework for multichannel despeckling," *IEEE J. Sel. Topics Appl. Earth Observ. Remote Sens.*, vol. 12, no. 8, pp. 2989–3003, Aug. 2019.
- [11] J. Liu, X. Qiu, L. Huang, and C. Ding, "Curved-path SAR geolocation error analysis based on BP algorithm," *IEEE Access*, vol. 7, pp. 20337–20345, Feb. 2019.
- [12] Q. Feng, D. An, H. Xie, and X. Huang, "Fast factorized back projection algorithm for bistatic forward-looking low frequency ultra wide band SAR imaging," *J. Electron. Inf. Technol.*, vol. 38, no. 4, pp. 941–949, Apr. 2016.
- [13] X. Zhang, P. Yang, and W. Ying, "BP algorithm for the multireceiver SAS," *IET Radar Sonar Navig.*, vol. 13, no. 5, pp. 830–838, May 2019.
- [14] J. Tang, Y. Deng, R. Wang, and N. Li, "Bulk-FFBP: Fast factorized back-projection algorithm based on range bulk processing," *J. Electron. Inf. Technol.*, vol. 39, no. 2, pp. 405–411, Feb. 2017.
- [15] Y. Miao, J. Wu, Z. Li, and J. Yang, "A generalized wavefront-curvature-corrected polar format algorithm to focus bistatic SAR under complicated flight paths," *IEEE J. Sel. Topics Appl. Earth Observ. Remote Sens.*, vol. 13, pp. 3757–3771, Jun. 2020.
- [16] C. Li *et al.*, "Focusing the L-band spaceborne bistatic SAR mission data using a modified RD algorithm," *IEEE Trans. Geosci. Remote Sens.*, vol. 58, no. 1, pp. 294–306, Jan. 2020.
- [17] X. Zhang, J. S. Tang, and H. P. Zhong, "Multireceiver correction for the chirp scaling algorithm in synthetic aperture sonar," *IEEE J. Ocean. Eng.*, vol. 39, no. 3, pp. 472–481, Jul. 2014.
- [18] W. Liu, G. Sun, X. Xia, D. You, M. Xing, and Z. Bao, "Highly squinted MEO SAR focusing based on extended omega-k algorithm and modified joint time and doppler resampling," *IEEE Trans. Geosci. Remote Sens.*, vol. 57, no. 11, pp. 9188–9200, Nov. 2019.
- [19] X. Qiu, D. Hu, and C. Ding, "An omega-k algorithm with phase error compensation for bistatic SAR of a translational invariant case," *IEEE Trans. Geosci. Remote Sens.*, vol. 46, no. 8, pp. 2224–2232, Aug. 2018.
- [20] F. Rosu, A. Anghel, R. Cacoveanu, B. Rommen, and M. Datcu, "Multiaperture focusing for spaceborne transmitter/ground-based receiver bistatic SAR," *IEEE J. Sel. Topics Appl. Earth Observ. Remote Sens.*, vol. 13, pp. 5823–5832, Oct. 2020.
- [21] R. Wang *et al.*, "Processing the azimuth-variant bistatic SAR data by using monostatic imaging algorithms based on two-dimensional principle of stationary phase," *IEEE Trans. Geosci. Remote Sens.*, vol. 49, no. 10, pp. 3504–3520, Oct. 2011.

- [22] H. Wu, F. Zhang, J. Tang, and Y. Tong, "An imaging algorithm based on the reference range history for the multiple receivers synthetic aperture sonar," *J. Electron. Inf. Technol.*, vol. 43, no. 3, pp. 650–656, Mar. 2021.
- [23] R. Wang, O. Loffeld, H. Nies, S. Knedlik, and J. H. G. Ender, "Chirp-scaling algorithm for bistatic SAR data in the constant-offset configuration," *IEEE Trans. Geosci. Remote Sens.*, vol. 47, no. 3, pp. 952–964, Mar. 2009.
- [24] R. Wang, O. Loffeld, Q. Ul-Ann, H. Nies, A. M. Orti, and A. Samarah, "A bistatic point target reference spectrum in the presence of trajectory deviations," *IEEE Geosci. Remote Sens. Lett.*, vol. 5, no. 3, pp. 517–521, Jul. 2008.
- [25] R. Wang, O. Loffeld, H. Nies, A. M. Ortiz, and S. Knedlik, "Bistatic point target reference spectrum in the presence of trajectory deviations," *IET Radar Sonar Navig.*, vol. 3, no. 2, pp. 177–185, Feb. 2009.
- [26] R. Wang, O. Loffeld, Y. L. Neo, H. Nies, and Z. Dai, "Focusing spaceborne/airborne hybrid bistatic SAR data using wavenumber-domain algorithm," *IEEE Trans. Geosci. Remote Sens.*, vol. 47, no. 7, pp. 2775–2783, Jul. 2009.
- [27] Q. Dong, Z. Yang, Z. Li, G. Sun, and M. Xing, "Wavenumber-domain imaging algorithm for high squint SAR based on azimuth variation range model," *J. Electron. Inf. Technol.*, vol. 38, no. 12, pp. 3166–3173, Dec. 2016.
- [28] X. Zhang, X. Chen, and W. Qu, "Influence of the stop-and-hop assumption on synthetic aperture sonar imagery," in *Proc. Int. Conf. Commun. Technol.*, Chengdu, China, Oct. 2017, pp. 1601–1607.
- [29] Y. Pailhas, S. Dugelay, and C. Capus, "Impact of temporal doppler on synthetic aperture sonar imagery," *J. Acoust. Soc. Amer.*, vol. 143, no. 1, pp. 318–329, Jan. 2018.
- [30] R. K. Raney, "A new and fundamental fourier transform pair," in *Proc. IEEE Int. Geosci. Remote Sens. Symp.*, Clear Lake, TX, USA, May 1992, pp. 106–107.
- [31] H. Zhang *et al.*, "Spaceborne/stationary bistatic SAR imaging with TerraSAR-X as an illuminator in staring-spotlight mode," *IEEE Trans. Geosci. Remote Sens.*, vol. 54, no. 9, pp. 5203–5216, Sep. 2016.
- [32] Y. Liu, Y. Zhou, Y. Zhou, L. Ma, B. Wang, and F. Zhang, "Accelerating SAR image registration using swarm-intelligent GPU parallelization," *IEEE J. Sel. Topics Appl. Earth Observ. Remote Sens.*, vol. 13, pp. 5694–5703, Sep. 2020.
- [33] S. Mislata and F. Silla, "Using remote accelerators to improve the performance of the FFTW library," in *Proc. IEEE Int. Conf. High Perform. Comput. Commun.*, Sydney, NSW, Australia, Dec. 2016, pp. 913–920.
- [34] Q. Wu, M. Xing, H. Shi, X. Hu, and Z. Bao, "Exact analytical two-dimensional spectrum for bistatic synthetic aperture radar in tandem configuration," *IEEE Trans. Geosci. Remote Sens.*, vol. 5, no. 3, pp. 349–360, Mar. 2011.



**Xuebo Zhang** (Member, IEEE) received the B.Eng. degree in electronic engineering and the Ph.D. degree in underwater acoustic engineering from Naval University of Engineering, Wuhan, China, in 2009, and 2014, respectively.

He is currently an Associate Professor with Northwest Normal University, Lanzhou, China. His research interests include synthetic aperture signal processing, array signal processing, and noise modeling.

Dr. Zhang is the Guest Editor for Special Issues of *Wireless Communications and Mobile Computing*,

*Electronics Letters*, and *MDPI Sensors*. He has been a Member of the Youth Editorial Board for *Journal of Electronics and Information Technology* since 2021.



**Haoran Wu** received the B.S., M.S., and Ph.D. degrees in underwater engineering from Naval University of Engineering, Wuhan, China, in 2011, 2014, and 2018, respectively.

He is currently a Lecturer with Naval University of Engineering, Wuhan, China. His current research interest includes underwater signal processing.



**Haixin Sun** (Member, IEEE) received the B.S. and M.S. degrees in electronic engineering from Shandong University of Science and Technology, Shandong, China, in 1999 and 2003, respectively, and the Ph.D. degree in communication engineering from Institute of Acoustic, Chinese Academy of Science, Shanghai, China, in 2006.

He visited the Department of Electrical and Computer Engineering, University of Connecticut, Storrs, CT, USA, from March 2012 to April 2013. He is currently a Professor and a Doctorial Advisor with the

School of Informatics, Xiamen University. His current research interests include underwater acoustic communication, and network and signal processing.

Dr. Sun is a member of IEICE. He was the recipient of the Huawei Fellowship of Xiamen University in 2010, the Faculty of Engineering Excellence Award of Xiamen University, and the Prize of Chinese Army Scientific and Technological in 2017. He has served for journals and conferences as a reviewer.



**Wenwei Ying** received the B.Eng. degree in electronic engineering from Ningbo University, Ningbo, China, in 2009, and the Ph.D. degree in communication engineering from the Naval University of Engineering, Wuhan, China, in 2013.

He is currently an Engineer with the Institute of Communication, Beijing, China. His current research interests include array signal processing, non-Gaussian signal processing, impulsive noise modeling, and VLF communication.